MATERIALS SCIENCE

Development of ferroelectric nematic fluids with giant-ε dielectricity and nonlinear optical properties

Jinxing Li[1†], Hiroya Nishikawa[2†], Junichi Kougo[1,3†], Junchen Zhou[1], Shuqi Dai[1], Wentao Tang[1], Xiuhu Zhao[1], Yuki Hisai[4], Mingjun Huang[1,3]*, Satoshi Aya[1,3]*

Superhigh-ε materials that exhibit exceptionally high dielectric permittivity are recognized as potential candidates for a wide range of next-generation photonic and electronic devices. In general, achieving a high-ε state requires low material symmetry, as most known high-ε materials are symmetry-broken crystals. There are few reports on fluidic high-ε dielectrics. Here, we demonstrate how small molecules with high polarity, enabled by rational molecular design and machine learning analyses, enable the development of superhigh-ε fluid materials (dielectric permittivity, $\varepsilon > 10^4$) with strong second harmonic generation and macroscopic spontaneous polar ordering. The polar structures are confirmed to be identical for all the synthesized materials. Furthermore, adapting this strategy to high–molecular weight systems allows us to generalize this approach to polar polymeric materials, creating polar soft matters with spontaneous symmetry breaking.

INTRODUCTION

High-ε dielectrics are classified as the materials exhibiting dielectric permittivity larger than 7 to 8 of silicon nitride. In recent decades, there emerges a new trend of high-ε electrics by using barium titanate–type (*1*–*5*) and two-dimensional (2D) crystalline materials (*6*–*8*), where ε reaches up to about 10^2 to 10^3, making it possible to realize electronics such as high energy-density dielectric films (*9*), high-performance capacitors (*10*) and insulators (*11*–*12*), and high-density memory (*13*). While barium titanate–type crystals serve as high-ε dielectrics owing to the breaking of the cubic symmetry in bulk, 2D crystals do so primarily because of the huge specific surface area of ordered atoms on the surface. These paradigms give a common perspective that the incidence of the high-ε state is only allowed when the symmetry of material is broken (thereby generally nonfluidic) and the thickness of the material is small, so that a net switchable polarization can remain at a high density and contribute to the high value of ε. Massive progress in this framework has been made in the past few decades, and it has been recognized that a majority of other materials, e.g., noncrystalline materials, are out of consideration for achieving a high-ε state because the two characteristics of broken symmetry and fluidity can barely coexist in the same material. Therefore, the selection variety of materials is considerably limited, so many other unknown properties may not show up so far.

Very recently, in 2017, two outliers appeared. One of our authors, Nishikawa *et al.* reported a new class of liquid crystalline phase state of matters, termed as polar nematic, that serves as the first example of fluidic superhigh-ε (or giant-ε) dielectric. The synthesized molecule, DIO (**5b** in Fig. 1), exhibits, e.g., $\varepsilon \sim 10^4$ at 1 kHz characterized by undefined polar structures and inherent high fluidity (*14*). At almost the same period, Mandle *et al.* (*15*–*18*) reported an unknown liquid crystalline phase state in RM734 (**1a** in Fig. 1), which has been assigned to be splay nematic later. Most recently, Chen *et al.* (*19*) confirmed that RM734 exhibits ferroelectric response. The previously unidentified nematic liquid crystal phases with a fascinating combination of huge ε and high fluidity are attracting the increasing endeavor for deep study in underlying physics and material properties (*20*–*22*).

Nevertheless, there are plenty of critical issues that need to be overcome to push the development of these materials for practical applications. Regarding the origin of polar nature, the structure and the mechanism of the phase formation are unclear and under debate, accompanying the uncertainty of the structural evolution pathway and the relationship with the conventional nematic phase. Moreover, with only the two aforementioned polar molecular systems experimentally proved by dielectric and optical nonlinear measurements, it is not sure whether this polar nematic state occurs occasionally or can be a generally accessible liquid crystal phase. To dissolve the erotetic arguments, we here establish a generic molecular guideline toward the rational design of giant-ε polar fluids with the aid of machine learning and make full analyses of polarizing optical microscopy (POM), second harmonic generation (SHG), and dielectric spectroscopy. We conclude that the emerging polar nematic state can widely exist in rod-shaped molecules under the proper conditions discussed below. We reveal the evolution of topological structures and unravel the family of the materials that provides a combination of outstanding performance of dielectricity (giant-ε) and second-order nonlinear optical (NLO) properties (high nonlinear coefficient). Furthermore, adopting this strategy to high–molecular weight systems additionally extends the polar material category from monomer to polymer. These results would promote the quicker development of a soft matter platform for high-performance fluidic dielectrics and nonlinear optics. Hereafter, because of the common ferroelectric nature for all the observed polar nematics, we unify the terms to be the ferroelectric nematic (N_F) phase after (*19*).

[1]South China Advanced Institute for Soft Matter Science and Technology (AISMST), School of Molecular Science and Engineering, South China University of Technology, Guangzhou 510640, China. [2]Physicochemical Soft Matter Research Team, RIKEN Center for Emergent Matter Science (CEMS), Japan. [3]Guangdong Provincial Key Laboratory of Functional and Intelligent Hybrid Materials and Devices, South China University of Technology, Guangzhou 510640, China. [4]Money Forward Inc. Shibaura, Minato-ku, Tokyo, Japan.
*Corresponding author. Email: huangmj25@scut.edu.cn (M.H.); satoshiaya@scut.edu.cn (S.A.)
†These authors contributed equally to this work.

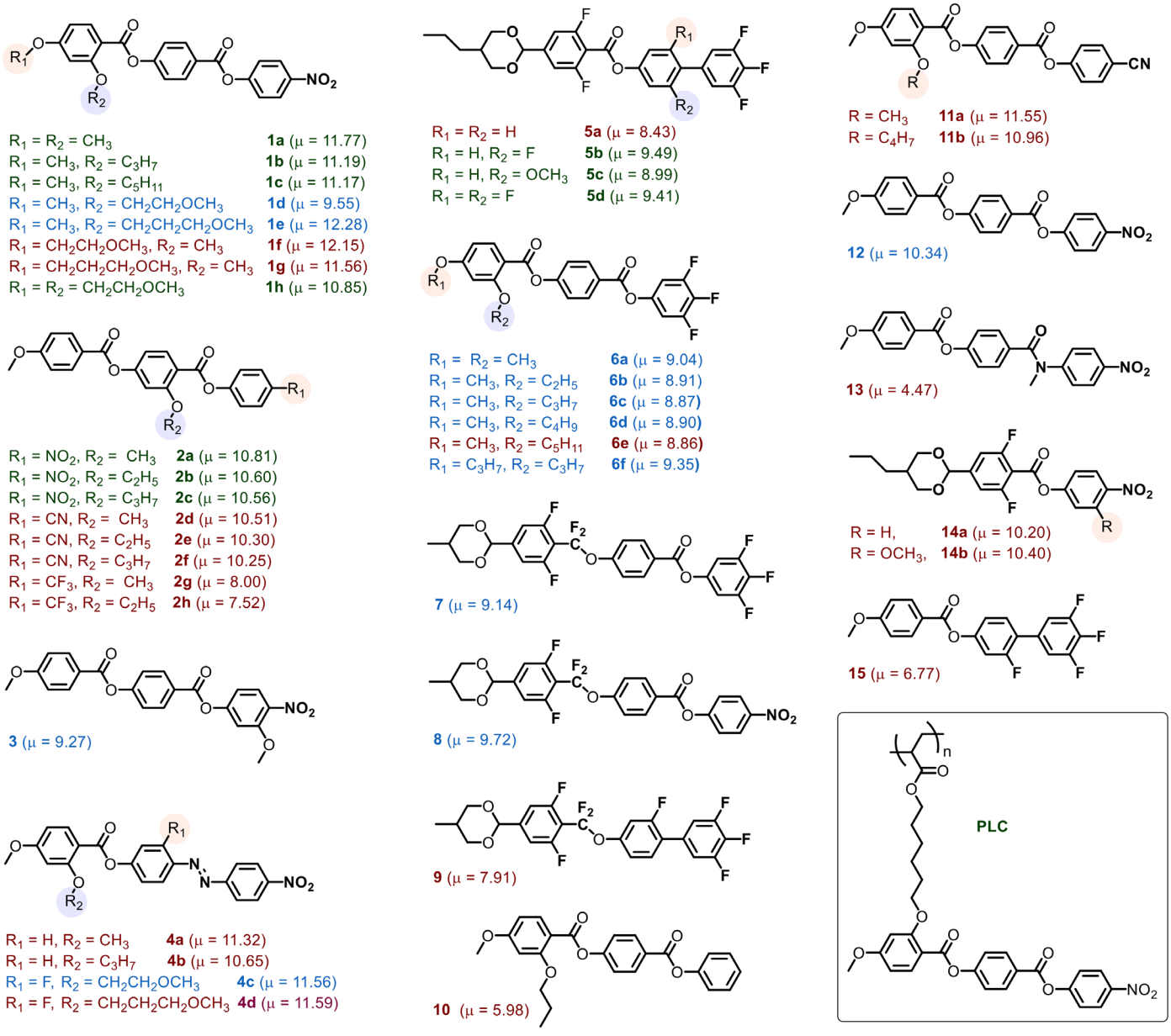

Fig. 1. Synthetic molecular library. All the synthesized materials are shown. The dipole moment values calculated by density functional theory are denoted. The compounds labeled by green color show stable N_F phase upon cooling process. The blue color label indicates observed metastable N_F phase; the red color label indicates no N_F phase observed at all temperatures upon cooling.

RESULTS AND DISCUSSION

Establishment of molecular library of the polar nematics guided by machine learning

To find generic molecular design for the N_F, we developed a custom machine learning algorithm (next section and discussion S4) to quantitatively extract molecular features that affect material function. This approach provides a guideline for synthesis and optimization of molecules to stabilize the N_F phase. We synthesized more than 40 new rod-shaped molecules with dipole moments (μ) ranging from 4 to 13 D (Fig. 1). Electron-withdrawing groups such as ester, fluoride, fluorocarbon ether, nitro, nitrile, or trifluorocarbon are arranged sequentially in the same direction to create large dipole moments. After careful examination by POM, SHG, and dielectric studies, these compounds can be divided into three categories according to the polar feature (highlighted as green, red, and blue colors in Fig. 1). For the compounds highlighted in green, the N_F phase could be stable at some temperatures upon cooling, with persistent existence of the typical N_F texture, large dielectric permittivity, and high SH signal. Two phase transitions (Iso→N→N_F) could also be identified by differential scanning calorimetry (DSC) measurement (table S1). In contrast, the compounds highlighted in red show either crystalline or traditional nonpolar N phase with extremely weak SH signal and low dielectric constant (ε < 15). The final class of compounds, highlighted in blue in Fig. 1, sits in between and exhibits a

metastable N_F phase. The fast crystallization within this category usually overwhelms the formation of the N_F phase, resulting in the N_F phase being overlooked under typical observation conditions during slow cooling. No N_F phase or related phase transitions could be observed in DSC with typical scanning rates of 1 to 30 K/min. However, we could expand the observation window of the N_F phase by suppressing crystal nucleation or decreasing the crystallization rate with appropriate treatment. For instance, quickly quenching to room temperature from the isotropic state helped us capture the N_F phase in most of these polar compounds, enabling the observation of characteristic POM texture and strong SH signal in a short time window (several seconds to tens of minutes). Overall, more than half of the synthesized materials (23 of 43) were detected to exhibit strong spontaneous polar ordering that results in huge dielectric permittivity, ε over 10,000 at all the frequencies below about 1 to 10 kHz. This strongly suggests that the N_F phase could be a general liquid crystalline state with a common structure and properties as discussed later. Note that, in contrast to the common ferroelectrics and relaxors that exhibit giant-ε in a narrow-frequency and narrow-temperature ranges, our synthesized materials present the giant dielectric permittivity in a wide range of frequency (<1 to 10 kHz) and temperature.

Molecular features for the polar nematics

Taking previously reported molecules with similar chemical structures or properties into account (fig. S1 and table S2), the total number of molecules for machine learning is expanded to ca. 70. The essential molecular features are summarized in Fig. 2A. The machine learning calculation is based on both the linear Pearson's correlation method (*23*) and the nonlinear analyses combining the random forest regression with a modified Shapley additive explanations (SHAP) analysis (*24*). Figure 2 (B and C) demonstrates the Pearson's correlation coefficients and SHAP values for the addressed parameters. The parameters carrying high Pearson's correlation coefficients to the stability of the N_F phase show wider distributions and higher absolute strength of SHAP value, confirming the importance of the parameters as below: molecular dipole > length > geometrical aspect ratio (AR) > angle of dipole moment; the rest of the parameters have negligible contributions. In addition, SHAP analysis provides a quantitative evaluation of the degree of positive or negative contribution of each parameter to the stability of the N_F phase. That is, the positive and negative values correspond to the stabilization and the destabilization effects on the N_F phase, respectively. Figure 2 (D to G) plots the SHAP values as a function of the molecular dipole, the geometrical AR, and the angle of dipole moment. The results offer a clear

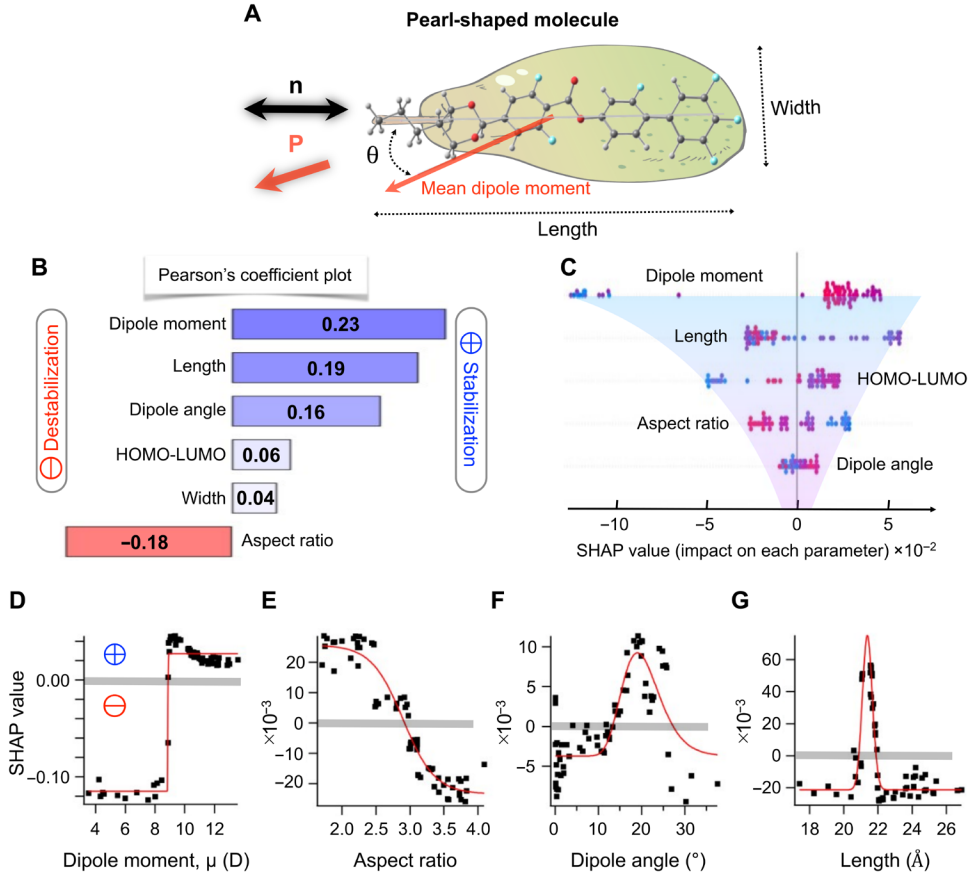

Fig. 2. Machine learning–driven understanding of molecular parameters stabilizing the N_F phase. (**A**) Molecular geometrical properties. As the model molecule, **5b** is shown. (**B**) Comparison of Pearson's correlation coefficient to the incidence of the N_F phase. Higher positive values mean higher probability to stabilize the N_F phase and vice versa. (**C**) The scattered plots of SHAP values for each molecular parameter. The colors of the points mean the magnitude of the parameters. Red-purple-blue colors correspond to the descending order of magnitude. This helps catch the tendency of how the magnitude correlate to the SHAP value. (**D** to **G**) The SHAP values as a function of the magnitude of each molecular parameter. The red lines are fitting curves by Hill equation. The crossover values from the negative to the positive regimes indicate the threshold values for stabilizing the N_F phase. HOMO, highest occupied molecular orbital; LUMO, lowest unoccupied molecular orbital.

statistical guideline for the molecular design of the N_F materials: (i) the dipole moment, $\mu > 9$ D; (ii) the geometrical AR defined as the length per the width, AR < 2.5; and (iii) the angle of the dipole should be in a moderate range, offering an oblique dipole (~20°). Note that all the conditions should be satisfied to guarantee the materials to exhibit both the high polarity and the liquid crystalline nature. For example, if the dipole moment is lower than the threshold of 9 D, then the traditional nonpolar nematic phase appears. This situation is supported by the prediction by Born (*25*) in 1916 that a ferroelectric anisotropic fluid would exist if the molecular dipole is large enough to overcome the thermal fluctuation. Meanwhile, the geometrical AR plays a crucial role in either avoiding material crystallization before transitioning into the N_F phase or expanding the temperature range of the N_F phase toward lower temperatures. Side-chain installation is synonymous with increasing the overall AR of mesogens, which proves to efficiently stabilize the N_F phase (e.g., compare end-chain substitution in **1f** and **1g** with side-chain substitution in **1d** and **1e**; Fig. 1). The longer the side-chain length, the lower the temperature at which the N_F phase is stable, as we observe in material series **1**, **2**, and **6**. Too long of a side chain may impede the parallel polar packing among rod-like mesogens and interrupt N_F formation as in **4d** and **6e**. The inclination of the dipole would work as the driving force for preventing the dimerization of the molecules. Otherwise, the molecules processing the dipole along the long axis universally show the traditional nematic phase, where the net dipole is zero through the dimerization. Noticeably, all the nitrile-containing molecules (e.g., **2d-f** and **11a-b**) fail to form the N_F phase, although with large dipole values (>10 D) and side groups. We speculate that the linear shape and small cross-sectional area of the nitrile group facilitate the dimerization between large dipoles, in strong contrast to the planar nitro group.

Structure, dielectricity, and polarity of the polar nematics

Revealing the topological structure of this new phase is crucial for understanding structure-property relationships. To date, the detailed structure of the N_F phase remains unclear, and how the structure is developed from the high-temperature N phase with the uniform director field is unknown. Note that while earlier works (*17*, *18*) have already triggered intensive theoretical studies (*20*–*22*), the true structure still requires further confirmation. To systematically correlate between the structures and the emergence of polarity, we simultaneously measured POM, SHG, and dielectric measurements for our synthesized materials upon varying temperature. While the dielectric permittivity provides information about the dynamic polarity where the polarization switches the direction following the electric field, the SH signal clarifies the static polarity where the polarization "freezes" during the incoming light field oscillations.

Figure 3 and figs. S4 and S5 demonstrate the systematic observations of POM, SHG, and dielectricity on three N_F materials including **5c**, **5b**, and **1a**. Notably, although all the synthesized N_F molecules have distinct chemical structures, they show common features on POM and DSC (table S1). They exhibit a similar structural evolution on cooling via four steps (Fig. 3, B to F): Schlieren texture (N phase)→stripe texture (N phase)→defect-free band texture (N phase)→band texture with line disclination (N_F phase). The similar texture evolution is also previously demonstrated in (*19*) [refer to figs. S8 and S9 and figures 2 and S11 in (*19*) for splay and band textures], suggesting the general structural pathway for the N_F materials. In general, from the isotropic state down to the middle of the N phase, the materials show relatively low dielectricity (e.g., $\varepsilon < 100$) and vanishingly small SH signal, similar to traditional N materials (Fig. 3A). However, as we further decrease temperature toward the N-N_F transition, both the dielectric permittivity and the SH signal grow continuously and markedly, confirming the emergence of the polar nature in the N phase as a pretransitional phenomenon. Curiously, the temperature window for the increase of the polarity is more than ca. 15°C in most of the N_F materials. In this range, we observe a structural transformation from Schlieren to a stripe texture, which runs parallel to the average molecular orientation (i.e., nematic director **n**). The stripe texture, attributed to the flexoelectric effect–induced splay deformation of the director field, enhances its contrast upon approaching the N-N_F transition (Figs. 3, C and D, and 4, D to F, and discussion S2). Right above the N-N_F transition, the stripe texture is replaced by the band texture without defects (Fig. 3, D and E), where filamentous regimes accompanied by different interference colors than the surroundings appear. This state is characterized by the sharpening of the Schlieren dark brushes and the continuous increase of both the dielectric permittivity and the SH signal, confirming the enhancement of both the structural ordering and polarity. Upon the transition to the N_F phase, a swarm of line defects pop up, seeded by the filamentous domains. In all the examined materials, each domain separated by the line defect is polar, emitting strong SH signal. The directional sense of the polarity is confirmed by SHG interferometry measurement. The SH signals from the neighboring domains interfere with a reference quartz plate in an opposite manner, i.e., one domain interferes constructively while the two neighboring domains do destructively (fig. S8). This confirms the nearly antiparallel polar sense of the adjacent domains, consistent with the conclusion of the ferroelectricity reported in (*19*). Note that the strong polarity in the N_F phase already develops at the stage of the defect-free band texture in the N phase, manifested by the drastic increase of the dielectricity and SH signal (Fig. 3). Dissimilar to the extinction of the N texture when the rubbing direction is parallel to either the polarizer or analyzer of the microscope, the domains of the N_F phase do not show complete extinction (Fig. 4, J to M, and figs. S7 and S11). Considering the overall structural evolution and SHG interferometry, the band texture in the N_F is attributed to a Néel type I director field accompanied by local bend deformation near the disclinations. The corresponding director field of the band texture (Fig. 4G) is also directly visualized by carefully observing the structural transition from the N_F phases to the N phase upon heating (Fig. 3G).

Figure 4 (A to I) summarizes the 3D model structures for N and N_F states, along with the corresponding textural features, dielectricity, and SHG characteristics. For understanding the POM observations of the N_F phase in detail, we consider several other possible N_F director field models that do not seemingly violate the experimental observations and the most plausible Néel type I director field: two wall-defect–type, Bloch-type, and two Néel-type models (fig. S10). Obviously, the band texture in the N_F phase cannot be explained by symmetric structures in a single band, i.e., wall-defect type and Néel type II structures should be excluded because the extinction area in the middle of each polarization domain cannot be observed in the experiment (fig. S11). We simulated the POM images for the structures and found that, while other structures including the Bloch-type defect display substantial discrepancy with the observed POM, only the Néel type I structure well reproduces the POM textures under various conditions (Fig. 4, J to M, and fig. S11). All the above

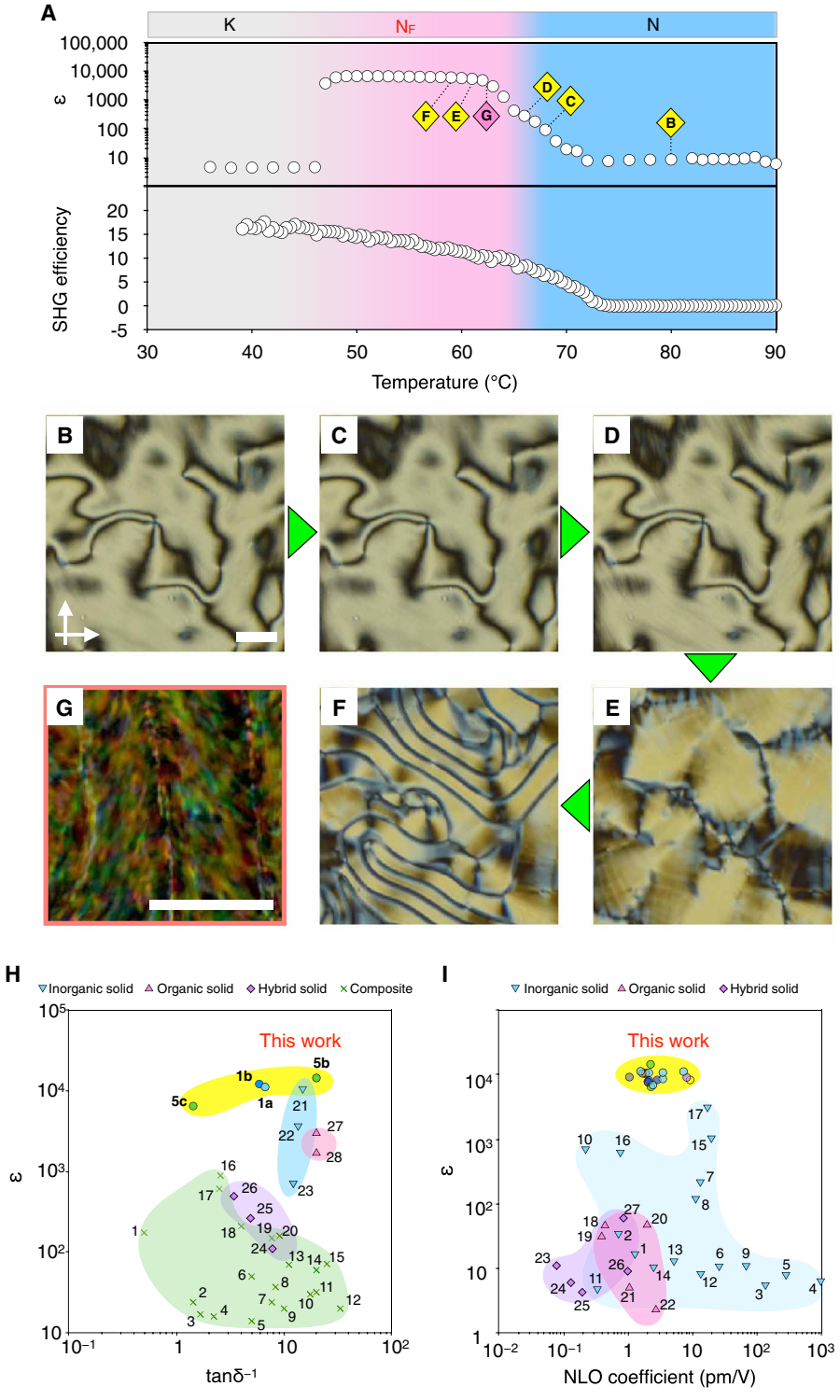

Fig. 3. Systematic studies of structure and polarity of the N_F phase POM, SHG, and dielectric spectroscopy. (**A**) The temperature dependencies of the dielectric constant and SHG efficiency. SHG efficiency is defined as the SHG intensity ratio of the N_F materials to that of the reference quartz plate. The corresponding POM images for **5c** (**B** to **G**) taken during cooling at various temperatures, indicated in (A). While the stripe texture in (D) exhibits the splay deformation in the sample plane, the band texture observed in (F) shows the bend deformation near the defect lines. The striped pattern in the band structure in (G), observed on heating, is considered as the embodiment of the Néel type I N_F structure. The cell thickness is 2.7 μm. Scale bars, 20 μm. Road maps of both the dielectric constant versus the loss tangent, $\tan\delta^{-1}$ (**H**), and dielectric constant versus NLO properties (**I**) are shown, respectively. The expanded view of (I) for the new N_F materials with their names is shown fig. S8. The colored areas mean the typical parameter range for different material groups: yellow, N_F materials; blue, inorganic solid materials; pink, organic solid materials; purple, hybrid solid materials; green, composite materials.

Texture feature	Nonpolar N	Local-polar N	Néel type I N_F
	Uniaxial alignment	Stripe texture	Band texture with disclination
Dielectricity, ε	1–100	100–1000	~ 10,000
SHG, ratio to quartz	<0.01	0.1–5	10–100

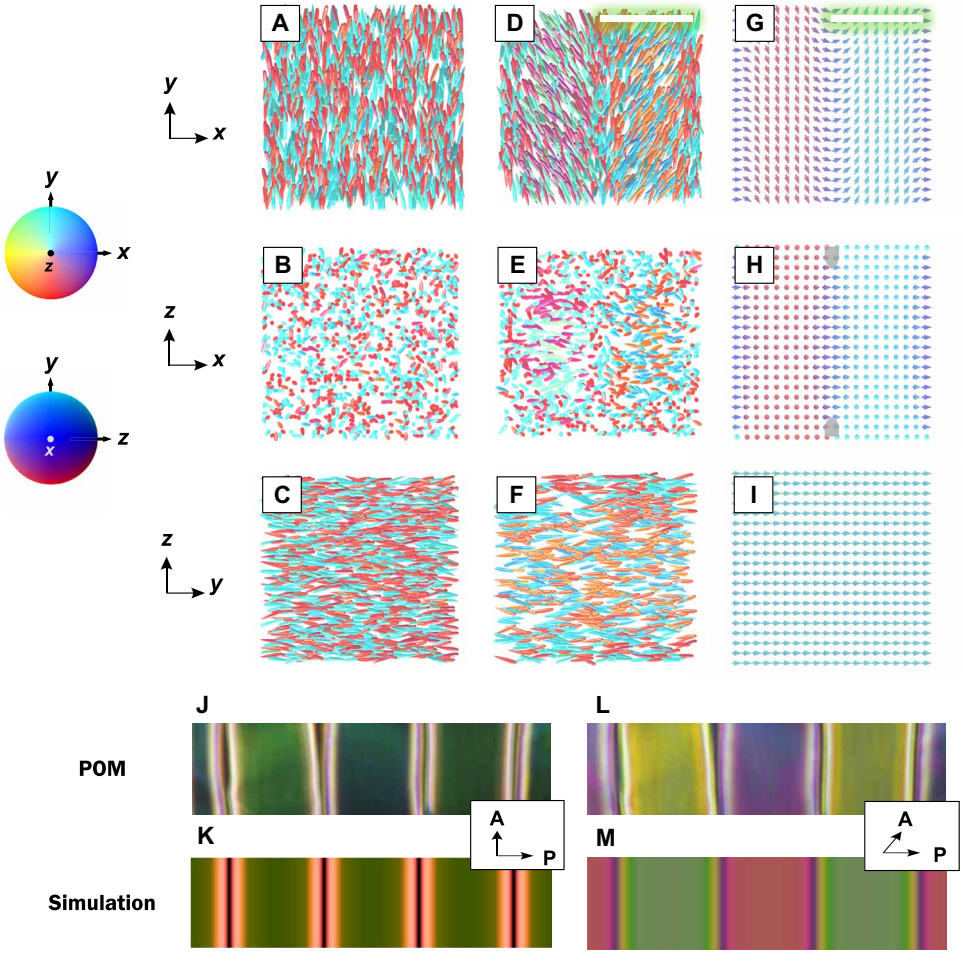

Fig. 4. Model and the free energy of the N_F phase. (**A** to **I**) The cross sections of the molecular orientational field of the homogeneous traditional N phase without polarity (A to C) and the locally polarized N phase with the splay texture (D to F) and the most plausible director field for the N_F phase (G to I) in the *xy*, *yz*, and *xz* planes. The *y* and *z* axes are parallel to the rubbing and surface normal directions. The gray bullet-shaped objects in (H) represent the defect walls near the surfaces. The textural feature, dielectricity, and SHG signal as the ratio to the SH signal of the quartz crystal are shown in the top table. The colors of the rods and arrows correspond to different polar and azimuthal orientational angles as indicated in the color maps in the *xy* and *yz* planes. The scale bars for (D) to (F) and (G) and (H) represent the typical length scale for the molecular and the director modulations: The scale bar in (D) to (F) is in the range of 4 to 10 μm; the scale bar in (G) and (H) is in the range of 20 to 70 μm. (**J** to **M**) The comparison of the experimental and calculated POM images of the Néel type I N_F structure under crossed and decrossed polarizers. The POM observation is made in a 5-μm cell. Image width, 145 μm.

evidence supports that the Néel type I structure is close to the "real" form of the N_F phase. More details of the N_F phase texture and structure evolution can be found in discussions S1 and S2. We note that potential detailed orientational states, smaller than several hundred nanometers in scale, may have been missed and will be the subject of future studies. Overall, our work more clearly elucidates packing structure in the N_F phase to better explore a broad range of physical effects, including response to external fields and topological defect change to diverse surface anchoring.

From polar nematic monomer to polymer

The small-molecule N_F phases described are metastable at room temperature and tend to crystallize, resulting in a loss in their high intrinsic polarity. Therefore, we considered further extending our approach to high–molecular weight side-chain polymers, where crystallization is unlikely to occur and mechanical properties potentially improved. On the basis of our newfound understanding of how AR influences the likelihood of N_F phase induction, we synthesized a side-chain polymer liquid crystal (PLC as in Fig. 1). PLC not

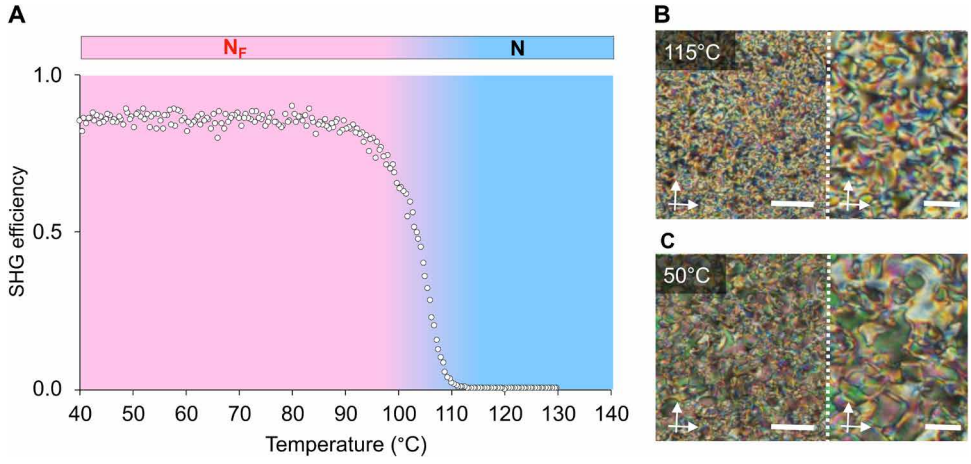

Fig. 5. Polar nematic polymer material. (**A**) SHG efficiency as a function of temperature. POM texture of polar polymer at 115°C in the N phase (**B**) and at 50°C N_F phases (**C**) under crossed polarizers. Scale bars, 50 μm (left) and 20 μm (right).

only displays the expected N_F-like texture (Fig. 5C) but also emits a strong SH signal (Fig. 5A). With this material, we successfully fabricated free-standing polymer fibers and films exhibiting a similar N_F phase (fig. S15). In the fiber, we observed that the polar molecules spontaneously orient along the elongation axis.

Last, we highlight that the polar nematic materials exhibit giant dielectric permittivity and high nonlinear coefficients. Figure 3 (H and I) displays the dielectric permittivity versus $\tan\delta^{-1}$ and versus NLO coefficient, respectively, for various types of materials including inorganic-, organic-, hybrid-solid, and composite materials (see tables S3 and S4). The N_F materials (**1a**, **1b**, **5b**, **5c**, etc.) have highly superior properties of dielectric permittivity (ε over 10^4 below 10 kHz) and low $\tan\delta^{-1}$ ($0.05 < \tan\delta < 0.20$), which represent the state-of-the-art functionality in soft matters. The giant dielectricity in the N_F materials is even comparable to well-known inorganic ferroelectric or relaxor materials (e.g., barium titanate crystals; see tables S3 and S4). Besides, for the N_F materials, one can notice that the high NLO coefficient ranging between 1 and 10 pm V^{-1}, which are comparable to some ferroelectric organic and hybrid solids. Note that those excellent NLO materials based on inorganics usually show quite low dielectric permittivity below 10. Hence, the excellent combination of giant dielectricity and NLO properties in the N_F materials, together with the fluidity or flexibility, is rather unique and offers vast technological potentials for high-performance supercapacitors, NLO elements, memory device, and electro-optic functional devices.

MATERIALS AND METHODS

Material synthesis

Refer to the Materials and Methods in the Supplementary Materials.

SHG measurement

We use a fundamental beam from a Q-switched pulsed laser (MPL-III-1064-20μJ) with a central wavelength of 1064 nm, maximum power of 200 mW, pulse duration of 5 ns, and 100-Hz repetition. The p-polarized fundamental beam was directed at liquid crystal cells. The SH light is detected at p-polarization from the transmission direction by a photomultiplier tube (DH-PMT-D100V, Daheng Optics). The time evolution of the SH signal is read by an oscilloscope, and the data are transferred to a computer. The SH signal is recorded every 1°C under the control of a homemade LabVIEW program. The schematics of the optical system are drawn in fig. S12. The nonlinear coefficient is calculated by the maker fringe method. The symmetry of the N_F phase is $C_{\infty v}$, giving spontaneous polarization mainly along the long molecular axis. The second-order NLO tensor is given by

$$\boldsymbol{d} = \begin{pmatrix} 0 & 0 & 0 & 0 & d_{15} & 0 \\ 0 & 0 & 0 & d_{24} & 0 & 0 \\ d_{31} & d_{32} & d_{33} & 0 & 0 & 0 \end{pmatrix}.$$

The second-order nonlinear polarizations (P_x, P_y, and P_z) are calculated as below

$$P_x(2\omega) = 2\varepsilon_0 d_{15} E_x(\omega) E_z(\omega)$$

$$P_y(2\omega) = 2\varepsilon_0 d_{24} E_y(\omega) E_z(\omega)$$

$$P_z(2\omega) = \varepsilon_0 d_{31} E_x(\omega)^2 + \varepsilon_0 d_{32} E_y(\omega)^2 + \varepsilon_0 d_{33} E_z(\omega)^2$$

$$P_x(2\omega) = \varepsilon_0 \chi_{15} E_x(\omega) E_z(\omega)$$

$$P_y(2\omega) = \varepsilon_0 \chi_{24} E_y(\omega) E_z(\omega)$$

$$P_z(2\omega) = \varepsilon_0 \chi_{31} E_x(\omega)^2/2 + \varepsilon_0 \chi_{32} E_y(\omega)^2/2 + \varepsilon_0 \chi_{33} E_z(\omega)^2/2$$

ω, ε_0, E_x, E_y, and E_z represent the frequency of the light, free-space permittivity, and three components of the electric field in the x, y, and z directions. In the polarization combinations of (polarization of excitation light, polarization of detected light) = (p,s), (s,s), (s,p), and (p,p), the probed polarizations are

$$P_y(2\omega) = 0 \text{ in (p, s) combination}$$

$$P_y(2\omega) = 0 \text{ in (s, s) combination}$$

$$P_x(2\omega) = 0, P_z(2\omega) = \varepsilon_0 \chi_{32} E_y(\omega)^2/2 \text{ in (s,p) combination}$$

$$P_x(2\omega) = \varepsilon_0 \chi_{15} E_x(\omega) E_z(\omega), P_z(2\omega) = \varepsilon_0 \chi_{31} E_x(\omega)^2/2$$
$$\text{in (p,p) combination}$$

In accordance with the above analyses, we observe strong SH signals in (s,p) and (p,p) combinations, and the rest only show negligible signals.

Machine learning

The code for the machine learning is written in Python by combining the following libraries and packages: Pandas data analysis library, NumPy extension module for numerical calculation, Matplotlib and Seaborn for statistical data visualization, SHAP package, and scikit-learn machine learning library. Refer to discussion S4 and fig. S13 for the detailed algorithm.

Berreman 4 × 4 matrix optical simulation

We perform the Berreman 4 × 4 matrix optical simulation (*26*) to find the adequate model structure that matches the real POM observation. Numerical simulations are made on the basis of the director structure as shown in fig. S11. We use the refractive indices of **5b** with ordinary and extraordinary refractive indices of $n_0 = 1.485$ and $n_e = 1.697$ without dispersion. The liquid crystal material is assumed to be composed of a stack of 100-nm-thick thin layers. To reproduce the color of the illumination halogen lamp, we use a measured spectrum of a halogen lamp and create 60 discrete different wavelengths evenly distributed between 380 and 780 nm. The simulation results are obtained as red-green-blue images by using color-matching functions for the 60 wavelengths.

SUPPLEMENTARY MATERIALS

Supplementary material for this article is available at http://advances.sciencemag.org/cgi/content/full/7/17/eabf5047/DC1

REFERENCES AND NOTES

1. B. Wul, Dielectric constants of some titanates. *Nature* **156**, 480 (1945).
2. W. Jackson, W. Reddish, High permittivity crystalline aggregates. *Nature* **156**, 717 (1945).
3. P. R. Coursey, K. G. Brand, Dielectric constants of some titanates. *Nature* **157**, 297–298 (1946).
4. M. G. Harwood, P. Popper, D. F. Rushman, Curie point of barium titanate. *Nature* **160**, 58–59 (1947).
5. B. T. Matthias, Dielectric constant and piezo-electric resonance of barium titanate crystals. *Nature* **161**, 325–326 (1948).
6. M. Osada, Y. Ebina, H. Funakubo, S. Yokoyama, T. Kiguchi, K. Takada, T. Sasaki, High-κ dielectric nanofilms fabricated from titania nanosheets. *Adv. Mater.* **18**, 1023–1027 (2006).
7. Y. Y. Illarionov, T. Knobloch, M. Jech, M. Lanza, D. Akinwande, M. I. Vexler, T. Mueller, M. C. Lemme, G. Fiori, F. Schwierz, T. Grasser, Insulators for 2D nanoelectronics: The gap to bridge. *Nat. Commun.* **11**, 3385 (2020).
8. T. Li, T. Tu, Y. Sun, H. Fu, J. Yu, L. Xing, Z. Wang, H. Wang, R. Jia, J. Wu, C. Tan, Y. Liang, Y. Zhang, C. Zhang, Y. Dai, C. Qiu, M. Li, R. Huang, L. Jiao, K. Lai, B. Yan, P. Gao, H. Peng, A native oxide high-κ gate dielectric for two-dimensional electronics. *Nat. Electron.* **3**, 473–478 (2020).
9. H. Pan, F. Li, Y. Liu, Q. Zhang, M. Wang, S. Lan, Y. Zheng, J. Ma, L. Gu, Y. Shen, P. Yu, S. Zhang, L.-Q. Chen, Y.-H. Lin, C.-W. Nan, Ultrahigh–energy density lead-free dielectric films via polymorphic nanodomain design. *Science* **365**, 578–582 (2019).
10. S. K. Kim, S. W. Lee, J. H. Han, B. Lee, S. Han, C. S. Hwang, Capacitors with an equivalent oxide thickness of <0.5 nm for nanoscale electronic semiconductor memory. *Adv. Funct. Mater.* **20**, 2989–3003 (2010).
11. D. Ji, T. Li, Y. Zou, M. Chu, K. Zhou, J. Liu, G. Tian, Z. Zhang, X. Zhang, L. Li, D. Wu, H. Dong, Q. Miao, H. Fuchs, W. Hu, Copolymer dielectrics with balanced chain-packing density and surface polarity for high-performance flexible organic electronics. *Nat. Commun.* **9**, 2339 (2018).
12. J. Robertson, High dielectric constant gate oxides for metal oxide Si transistors. *Rep. Prog. Phys.* **69**, 327–396 (2006).
13. C.-H. Lee, S.-H. Hur, Y.-C. Shin, J.-H. Choi, D.-G. Park, K. Kim, Charge-trapping device structure of SiO2/SiN/high-*k* dielectric Al2O3 for high-density flash memory. *Appl. Phys. Lett.* **86**, 152908 (2005).
14. H. Nishikawa, K. Shiroshita, H. Higuchi, Y. Okumura, Y. Haseba, S. Yamamoto, K. Sago, H. Kikuchi, A fluid liquid-crystal material with highly polar order. *Adv. Mater.* **20**, 1702354 (2017).
15. R. J. Mandle, S. J. Cowling, J. W. Goodby, A nematic to nematic transformation exhibited by a rod-like liquid crystal. *Phys. Chem. Chem. Phys.* **19**, 11429–11435 (2017).
16. R. J. Mandle, S. J. Cowling, J. W. Goodby, Rational design of rod-like liquid crystals exhibiting two nematic phases. *Chemistry* **23**, 14554–14562 (2017).
17. A. Mertelj, L. Cmok, N. Sebastián, R. J. Mandle, R. R. Parker, A. C. Whitwood, J. W. Goodby, M. Čopič, Splay nematic phase. *Phys. Rev. X* **8**, 041025 (2018).
18. N. Sebastián, L. Cmok, R. J. Mandle, M. R. de la Fuente, I. D. Olenik, M. Čopič, A. Mertelj, Ferroelectric-ferroelastic phase transition in a nematicliquid crystal. *Phys. Rev. Lett.* **124**, 037801 (2020).
19. X. Chen, E. Korblova, D. Dong, X. Wei, R. Shao, L. Radzihovsky, M. A. Glaser, J. E. Maclennan, D. Bedrov, D. M. Walba, N. A. Clark, First-principles experimental demonstration of ferroelectricity in a thermotropic nematic liquid crystal: Polar domains and striking electro-optics. *Proc. Natl. Acad. Sci. U.S.A.* **117**, 14021–14031 (2020).
20. N. Chaturvedi, R. D. Kamien, Mechanisms to splay-bend nematic phases. *Phys. Rev. E* **100**, 022704 (2019).
21. M. Copic, A. Mertelj, Q-tensor model of twist-bend and splay nematic phases. *Phys. Rev. E* **101**, 022704 (2020).
22. M. P. Rosseto, J. V. Selinger, Theory of the splay nematic phase: Single vs. double splay. *Phys. Rev. E* **101**, 052707 (2020).
23. S. M. Stigler, Francis Galton's account of the invention of correlation. *Stat. Sci.* **4**, 73–79 (1989).
24. S. M. Lundber, S.-I. Lee, A unified approach to interpreting model predictions, in *NIPS'17: Proceedings of the 31st International Conference on Neural Information Processing Systems* (ACM, 2017), pp. 4768–4777.
25. M. Born, Über anisotrope Flüssigkeiten. Versuch einer Theorie der flüssigen Kristalle und des elektrischen Kerr-Effekts in Flüssigkeiten. Sitzungsber. *Preuss. Akad Wiss.* **30**, 614–645 (1916).
26. D. W. Berreman, Optics in stratified and anisotropic media: 4×4-matrix formulation. *J. Opt. Soc. Am.* **62**, 502–510 (1972).
27. M., Gil, Preparation of bis(benzenecarboxamides) as calcium channel blockers. PCT Int. Appl., 2007068754 (2007).
28. S. Kawashita, K. Aoyagi, H. Yamanaka, R. Hantani, S. Naruoka, A. Tanimoto, Y. Hori, Y. Toyonaga, K. Fukushima, S. Miyazaki, Y. Hantani, Symmetry-based ligand design and evaluation of small molecule inhibitors of programmed cell death-1/programmed death-ligand 1 interaction. *Bioorg. Med. Chem. Lett.* **29**, 2464–2467 (2019).
29. A. K. Al-Lami, Preparation and mesomorphic characterization of supramolecular hydrogen-bonded dimer liquid crystals. *Polycycl. Aromat. Compd.* **36**, 197–212 (2015).
30. D. Ndaya, R. Bosirea, R. M. Kasi, Cholesteric–azobenzene liquid crystalline copolymers: Design, structure and thermally responsive optical properties. *Polym. Chem.* **10**, 3868–3878 (2019).
31. J. Pecyna, P. Kaszynski, B. Ringstrand, M. Bremer, Investigation of high Δε derivatives of the [closo-1-CB9H10]–anion for liquid crystal display applications. *J. Mater. Chem. C* **2**, 2956–2964 (2014).
32. M.-J. Gim, D. A. Beller, D. K. Yoon, Morphogenesis of liquid crystal topological defects during the nematic-smectic A phase transition. *Nat. Commun.* **8**, 15453 (2017).
33. A. Liaw, M. Wiener, "Classification and Regression by randomForest," *R News*, ISSN 1609-3631.
34. C. Wu, X. Huang, X. Wu, J. Yu, L. Xie, P. Jiang, TiO2-nanorod decorated carbon nanotubes for high-permittivity and low-dielectric-loss polystyrene composites. *Compos. Sci. Technol.* **72**, 521–527 (2012).
35. Y. Chen, Q. Zhuang, X. Liu, J. Liu, S. Lin, Z. Han, Preparation of thermostable PBO/graphene nanocomposites with high dielectric constant. *Nanotechnology* **24**, 245702 (2013).
36. K. Hayashida, Dielectric properties of polymethacrylate-grafted carbon nanotube composites. *RSC Adv.* **3**, 221–227 (2013).
37. L. J. Romasanta, M. Hernández, M. A. López-Manchado, R. Verdejo, Functionalised graphene sheets as effective high dielectric constant fillers. *Nanoscale Res. Lett.* **6**, 508 (2011).
38. M. Panda, V. Srinivas, A. K. Thakur, On the question of percolation threshold in polyvinylidene fluoride/nanocrystalline nickel composites. *Appl. Phys. Lett.* **92**, 132905 (2008).
39. J. Yuan, S. Yao, W. Li, A. Sylvestre, J. Bai, Vertically aligned carbon nanotube arrays on SiC microplatelets: A high figure-of-merit strategy for achieving large dielectric constant and low loss in polymer composites. *J. Phys. Chem. C* **118**, 22975–22983 (2014).

40. A. B. Dichiara, J. Yuan, S. Yao, A. Sylvestre, L. Zimmer, J. Bai, Effective synergistic effect of Al2O3and SiC microparticles on the growth of carbon nanotubes and their application in high dielectric permittivity polymer composites. *J. Mater. Chem. A* **2**, 7980–7987 (2014).
41. C. Han, A. Gu, G. Liang, L. Yuan, Carbon nanotubes/cyanate ester composites with low percolation threshold, high dielectric constant and outstanding thermal property. *Compos. Part A Appl. Sci. Manuf.* **41**, 1321–1328 (2010).
42. J. Y. Kim, T. Y. Kim, J. W. Suk, H. Chou, J.-H. Jang, J. H. Lee, I. N. Kholmanov, D. Akinwande, R. S. Ruoff, Enhanced dielectric performance in polymer composite films with carbon nanotube-reduced graphene oxide hybrid filler. *Small* **10**, 3405–3411 (2014).
43. G. Tian, J. Song, J. Liu, S. Qi, D. Wu, Enhanced dielectric permittivity and thermal stability of graphene-polyimide nanohybrid films. *Soft Mater.* **12**, 290–296 (2014).
44. C. R. Yu, D.-M. Wu, Y. Liu, H. Qiao, Z.-Z. Yu, A. Dasari, X. Du, Y.-W. Mai, Electrical and dielectric properties of polypropylene nanocomposites based on carbon nanotubes and barium titanate nanoparticles. *Compos. Sci. Technol.* **71**, 1706–1712 (2011).
45. A. Ameli, S. Wang, Y. Kazemi, C. B. Park, P. Pötschke, A facile method to increase the charge storage capability of polymer nanocomposites. *Nano Energy* **15**, 54–65 (2015).
46. P. Kim, N. M. Doss, J. P. Tillotson, P. J. Hotchkiss, M.-J. Pan, S. R. Marder, J. Li, J. P. Calame, J. W. Perry, High energy density nanocomposites based on surface-modified BaTiO3 and a ferroelectric polymer. *ACS Nano* **3**, 2581–2592 (2009).
47. K. Yu, H. Wang, Y. Zhou, Y. Bai, Y. Niu, Enhanced dielectric properties of BaTiO3/ poly(vinylidene fluoride) nanocomposites for energy storage applications. *J. Appl. Phys.* **113**, 034105 (2013).
48. K. S. Lam, Y. W. Wong, L. S. Tai, Y. M. Poon, F. G. Shin, Dielectric and pyroelectric properties of lead zirconate titanate/polyurethane composites. *J. Appl. Phys.* **96**, 3896–3899 (2004).
49. L. Zhang, X. Shan, P. Wu, Z. Y. Cheng, Dielectric characteristics of CaCu3Ti4O12/P(VDF-TrFE) nanocomposites. *Appl. Phys. A Mater. Sci. Process.* **107**, 597–602 (2012).
50. H. Tang, Y. Lin, H. A. Sodano, Synthesis of high aspect ratio BaTiO3Nanowires for high energy density nanocomposite capacitors. *Adv. Energy Mater.* **3**, 451–456 (2013).
51. M. Arbatti, X. Shan, Z. Cheng, Ceramic-polymer composites with high dielectric constant. *Adv. Mater.* **19**, 1369–1372 (2007).
52. Y. Jin, N. Xia, R. A. Gerhardt, Enhanced dielectric properties of polymer matrix composites with BaTiO3 and MWCNT hybrid fillers using simple phase separation. *Nano Energy* **30**, 407–416 (2016).
53. S. Luo, S. Yu, R. Sun, C.-P. Wong, Nano Ag-deposited BaTiO3 hybrid particles as fillers for polymeric dielectric composites: Toward high dielectric constant and suppressed Loss. *ACS Appl. Mater. Interfaces* **6**, 176–182 (2014).
54. M. A. Subramanian, A. W. Sleight, ACu3Ti4O12 and ACu3Ru4O12 perovskites: High dielectric constants and valence degeneracy. *Solid State Sci.* **4**, 347–351 (2002).
55. R. Kumari, R. Seera, A. De, R. Ranjan, T. N. Guru Row, Organic multifunctional materials: Second harmonic, ferroelectric, and dielectric properties in *N*-benzylideneaniline analogues. *Cryst. Growth Des.* **19**, 5934–5944 (2019).
56. S. Horiuchi, F. Ishii, R. Kumai, Y. Okimoto, H. Tachibana, N. Nagaosa, Y. Tokura, Ferroelectricity near room temperature in co-crystals of nonpolar organic molecules. *Nat. Mater.* **4**, 163–166 (2005).
57. M. J. Weber, *Handbook of Optical Materials 1.9.3 Second Harmonic Generation Coefficients* (CRC Press, 2003).
58. J. Link, J. Fontanella, C. G. Andeen, Temperature variation of the dielectric properties of bismuth germanate and bismuth germanium oxide. *J. Appl. Phys.* **51**, 4352–4355 (1980).
59. M. Delfino, G. M. Loiacono, W. A. Smith, Thermal and dielectric properties of LiKSO4 and LiCsSO4. *J. Solid State Chem.* **31**, 131–134 (1980).
60. A. Chevy, A. Segura, V. Muñoz, Effects of pressure and temperature on the dielectric constant of gas, gase, and inse: Role of the electronic contribution. *Phys. Rev. B* **60**, 15866–15874 (1999).
61. D. Berlincourt, H. Jaffe, L. R. Shiozawa, Electroelastic properties of the sulfides, selenides, and tellurides of zinc and cadmium. *Phys. Rev.* **129**, 1009–1017 (1963).
62. R. R. Neurgaonkar, W. K. Cory, Progress in photorefractive tungsten bronze crystals. *J. Opt. Soc. Am. B* **3**, 274–282 (1986).
63. A. U. Sheleg, V. G. Hurtavy, The influence of electron irradiation on the dielectric characteristics of single crystals of AgGaSe2. *Phys. Solid State* **61**, 1695–1698 (2019).
64. R. J. Pollina, C. W. Garland, Dielectric and ultrasonic measurements in CsH2AsO4. *Phys. Rev. B* **12**, 362–367 (1975).
65. A. De, K. V. Rao, Dielectric properties of synthetic quartz crystals. *J. Mater. Sci.* **23**, 661–664 (1988).
66. C. R. Raja, R. Gobinathan, F. D. Gnanam, Dielectric properties of beta barium borate and potassium pentaborate single crystals. *Cryst. Res. Technol.* **28**, 737–743 (1993).
67. S. W. Ko, D. A. Mourey, T. Clark, S. Trolier-Mckinstry, Synthesis, characterization, and dielectric properties of β-Gd2(MoO4)3 thin films prepared by chemical solution deposition. *J. Sol-Gel Sci. Technol.* **54**, 269–275 (2010).
68. M. Zgonik, R. Schlesser, I. Biaggio, E. Voit, J. Tscherry, P. Günter, Materials constants of KNbO3 relevant for electro- and acousto-optics. *J. Appl. Phys.* **74**, 1287–1297 (1993).
69. Y. Takagi, K. Gesi, Electrical properties of NaNO2 single crystal in the vicinity of the ferroelectric curie temperature. *J. Phys. Soc. Jpn.* **22**, 979–986 (1967).
70. A. El Ghandouri, S. Sayouri, T. Lamcharfi, A. Elbasset, Structural, microstructural and dielectric properties of Ba1-xLaxTi(1-x/4)O3 prepared by sol gel method. *J. Adv. Dielectr.* **9**, 1950026 (2019).
71. K. F. Young, H. P. R. Frederikse, Compilation of the static dielectric constant of inorganic solids. *J. Phys. Chem. Ref. Data Monogr.* **2**, 313–410 (1973).
72. M. Anis, S. P. Ramteke, M. D. Shirsat, G. G. Muley, M. I. Baig, Novel report on γ-glycine crystal yielding high second harmonic generation efficiency. *Opt. Mater.* **72**, 590–595 (2017).
73. A. N. Holden, W. J. Merz, J. P. Remeika, B. T. Matthias, Properties of guanidine aluminum sulfate hexahydrate and some of its isomorphs. *Phys. Rev.* **101**, 962–966 (1956).
74. J. W. Williams, C. H. Schwrzngel, The dielectric constants of binary mixtures. VI The electric moments of certain nitro derivatives of benzene and toluene. *J. Am. Chem. Soc.* **50**, 362–368 (1928).
75. G. Q. Mei, H. Y. Zhang, W. Q. Liao, A symmetry breaking phase transition-triggered high-temperature solid-state quadratic nonlinear optical switch coupled with a switchable dielectric constant in an organic-inorganic hybrid compound. *Chem. Commun.* **52**, 11135–11138 (2016).
76. J. Zhang, S. Han, X. Liu, Z. Wu, C. Ji, Z. Sun, J. Luo, A lead-free perovskite-like hybrid with above-room-temperature switching of quadratic nonlinear optical properties. *Chem. Commun.* **54**, 5614–5617 (2018).
77. W. Q. Liao, J. X. Gao, X. N. Hua, X. G. Chen, Y. Lu, Unusual two-step sequential reversible phase transitions with coexisting switchable nonlinear optical and dielectric behaviors in [(CH3)3NCH2Cl]2[ZnCl4]. *J. Mater. Chem. C* **5**, 11873–11878 (2017).
78. S. P. Ramteke, M. I. Baig, M. Shkir, S. Kalainathan, M. D. Shirsat, G. G. Muley, M. Anisa, Novel report on SHG efficiency, Z-scan, laser damage threshold, photoluminescence, dielectric and surface microscopic studies of hybrid inorganic ammonium zinc sulphate hydrate single crystal. *Opt. Laser Technol.* **104**, 83–89 (2018).
79. I. Khan, M. Anis, U. Bhati, Influence of L-lysine on optical and dielectric traits of cadmium thiourea acetate complex crystal. *Optik* **170**, 43–47 (2018).

Acknowledgments: We thank P. Shieh for editing English of our manuscript. **Funding:** This work is supported by Guangdong Provincial Key Laboratory of Functional and Intelligent Hybrid Materials and Devices (no. 2019B121203003), The Recruitment Program of Guangdong (no. 2016ZT06C322), Major Program of National Natural Science Foundation of China (NSFC no. 51890871), the National Science Foundation of China for Young Scientists of China (NSFC no. 11904106), International (Regional) Cooperation And Exchange Project (NSFC no. 12050410231), and the Fundamental Research Funds for the Central Universities (no. 2019JQ05). **Author contributions:** S.A. and M.H. designed and directed the research. J.L., S.D., and M.H. synthesized all the materials. J.Z., H.N., and S.A. made structural and viscoelastic analyses. H.N., J.K., and S.A. made measurements and analyses of dielectric properties. J.K. and S.A. built measuring system for SHG and analyzed the data. X.Z. and S.A. made density functional theory calculation. Y.H. and S.A. wrote the codes for machine learning and made analyses of chemical structures. J.K. and S.A. wrote the codes for generating director field, calculated the free energy, and made optical simulation. S.A. and M.H. wrote the manuscript. All the authors discussed and amended the manuscript. **Competing interests:** The authors declare that they have no competing interests. **Data and materials availability:** All data needed to evaluate the conclusions in the paper are present in the paper and/or the Supplementary Materials. Additional data related to this paper may be requested from the corresponding authors.

Submitted 31 October 2020
Accepted 4 March 2021
Published 21 April 2021
10.1126/sciadv.abf5047

Citation: J. Li, H. Nishikawa, J. Kougo, J. Zhou, S. Dai, W. Tang, X. Zhao, Y. Hisai, M. Huang, S. Aya, Development of ferroelectric nematic fluids with giant-ε dielectricity and nonlinear optical properties. *Sci. Adv.* **7**, eabf5047 (2021).